Microphysical view of development and ice production of mid-latitude stratocumulus during an extratropical cyclone

Yuanmou Du[1,3], Dantong Liu[2], Delong Zhao[1,3], Mengyu Huang[1,3], Ping Tian[1,3], Dian Wen[1,3], Wei Xiao[1,3], Wei Zhou[1,3], Baiwan Pan[2], Dongfei Zuo[4], Xiange Liu[1,3], Yingying Jing[1,3], Rong Zhang[4], Jiujiang Sheng[1,3], Fei Wang[1,3], Yu Huang[1,3], Yunbo Chen[1,3], Deping Ding[1,3]

[1]Beijing Weather Modification Center, Beijing, 100089, China
[2]Department of Atmospheric Sciences, School of Earth Sciences, Zhejiang University, Hangzhou, Zhejiang, 310027, China
[3]Beijing Key Laboratory of Cloud, Precipitation and Atmospheric Water Resources, Beijing, 100089, China
[4]CMA Weather Modification Center, Beijing, 100081, China

Correspondence to: dantongliu@zju.edu.cn

Abstract. The microphysical properties associated with the ice production importantly determine the precipitation rate of clouds. In this study, the microphysical properties including the size distribution and particle morphology of water and ice for stratocumulus during an extratropical cyclone over the northern China were in-situ characterized. Stages of cloud were investigated including young cells rich of liquid water, developing and mature stages with high number concentration of ice particles (N_{ice}). The N_{ice} could reach 300 L^{-1} at the mature stage, about two orders of magnitudes higher than the primary ice number concentration calculated from ice nucleation. This high N_{ice} occurred at about −5 to −12 ℃, spanning the temperature region of Hallett-Mossop process and possible other mechanisms for the secondary ice production (SIP). The N_{ice} was positively associated with the number concentrations of large graupel with diameter (d) > 250 μm and large supercooled droplet $(d$ > 50 μm). The SIP rate was 0.005-1.8 $L^{-1}s^{-1}$ derived from the measured N_{ice} with known ice growth rate between two sizes. The SIP rate could be produced by a simplified collision-coalescence model within an uncertainty factor of 5, by considering the collection of large droplets by graupel. The collection efficiency between was found to increase when the size of droplet was closer to graupel which may improve the agreement between measurement and model. Importantly, the overall N_{ice} was found to be highly related to the distance to cloud-top (DCT). The level with larger DCT had more abundant rimmed graupels falling from the above level, which promoted the coalescence processes between graupels and droplets, producing a higher fraction of smaller ice through SIP. This seeder-feeder process extended the avalanche SIP at lower temperature up to −14 ℃ beyond the temperature region of Hallett-Mossop process. The results illustrated the microphysical properties of clouds with convective cells under different stages, which will improve the understanding of the key processes in controlling the cloud glaciation and precipitation process.

1 Introduction

The mid-latitude clouds are mostly present in mixed-phase (Mülmenstädt et al., 2015). The microphysical properties associated
35   with the ice production or the conversation from liquid water to ice importantly determine the precipitation rate and lifetime
of clouds (Lau and Wu, 2003; Cantrell and Heymsfield, 2005). The growth rate of hydrometeors through ice phase is usually
more rapid than the warm rain process (Lohmann and Feichter, 2005; Mcfarquhar et al., 2017). Understanding the ice
production and glaciation process in clouds is important for more accurate parameterization of microphysical processes in
weather prediction models (Korolev et al., 2017; Bacer et al., 2021), and this needs to be understood in vertical dimension and
40   under different stages of cloud development (Zhao et al., 2019) .

In addition to the primary ice produced by homogeneous and heterogeneous nucleation processes from aerosol particles
(Kanji et al., 2017), the secondary ice production (SIP) process can rapidly produce high numbers of ice up to several orders
of magnitude more than that produced from ice nucleation (Mossop, 1985; Harris-Hobbs and Cooper, 1987; Field et al., 2016;
Korolev et al., 2022), which is an important process to accelerate the cloud glaciation. The SIP can occur under different
45   ambient temperatures through different processes including the rime splintering process , fragmentation during droplet freezing,
fragmentation due to ice–ice collision, ice particle fragmentation due to thermal shock, fragmentation of sublimating ice
particle, and the activation of ice-nucleating particles in transient supersaturation around freezing drops (Korolev et al., 2020).
The Hallett-Mossop (H-M) mechanism was well reproduced through laboratory work (Hallett and Mossop, 1974) and is
usually introduced to explain the high abundance of ice number concentration at slightly sub-freezing temperature (−3 to −8 ℃)
50   (Hogan et al., 2002; Huang et al., 2008; Crosier et al., 2013; Korolev et al., 2022), and the freshly formed ice mostly exhibited
the shapes of columns or needles (Locatelli et al., 2008; Crosier et al., 2011; Lloyd et al., 2014; Taylor et al., 2016), consistent
with the diffusion growth habit of ice under such temperature. However, the H-M process may not sufficiently explain the
even more rapid SIP rate in observation, the fragmentation during droplet freezing and ice-ice collision may play an important
role in the secondary ice production process (Rangno and Hobbs, 2001), it may also be formed by the growth of ice from the
55   outside into the H-M temperature zone (Field et al., 2016). Supercooled large drop may play important roles in the SIP process,
which can fracture when freezing and emit ice splinters (Lawson et al., 2015), and this process could extend the SIP to a lower
temperature on top of the convective core. A recent study also found SIP process could occur at temperature as low as −27 ℃
(Korolev et al., 2022).

Mid-latitude clouds formed from extratropical cyclone are the main sources of precipitations for the east Asia (Li et al.,
60   2016). The microphysical properties of clouds over the North China Pian have been observed during the frontal system (Yang
et al., 2017; Hou et al., 2021; Hou et al., 2023). It was found more ice particles close to the convective region and the SIP was
found to produce ice number concentration up to over 300 L^{-1}, which may promote the intensity of precipitation. These studies
suggest that the SIP process may be explained by the H-M process or other mechanisms, such as collisional fragmentation,
which may contribute to SIP in regions that do not fit the H-M criteria (Hou et al., 2023). However, the key factors in
65   controlling the SIP process and how these factors can influence the SIP at different stages of clouds have not been elucidated.

The cold front system formed by the merging of cold air from the rear of extratropical cyclones with the warm air mass brought in by the southwest warm and moist air along the edge of the subtropical high-pressure system is the main weather system that produces rainfall in northern China (Wang et al., 2014). This study therefore investigated the microphysical properties of a typical mid-latitude clouds formed via this typical weather system over the north China Plain through the aircraft
70   in-situ measurements. Stages of cloud were investigated including young cells rich of liquid water, developing and mature stages with high number concentration of ice particles. The key factors in controlling SIP are elucidated through the calculation from measurements and modelling.

2 Experiment

2.1 Instrumentation

75   The Kingair350 aircraft of Beijing weather modification center was employed for in-situ measurements in this experiment (Liu et al., 2020; Tian et al., 2020; Zuo et al., 2023). This experiment aimed to conduct continuous aircraft observations of clouds developed during an extratropical cyclone over the northern China. The goals were to obtain in-situ microphysical data of clouds during the development of frontal system and to study the production of ice in clouds. The experiment was designed based on numerical model forecasting results and real-time radar data. To capture the evolving microphysical characteristics
80   of stratocumulus clouds at various development stages, aircraft observational experiment was conducted in accordance with real-time changes in precipitation radar echoes.

In-situ temperature, relative humidity, wind speed and wind direction were measured by Aircraft Integrated Meteorological Measurement System (AIMMS20, Aventech Research Inc.) with a time resolution of 1 second (Beswick et al., 2008). Distribution of Aerosol particles ranged from 0.1 to 3 μm in diameter was measured by Passive Cavity Aerosol Spectrometer
85   Probe (PCASP, DMT Inc.) with a time resolution of 1 second (Cai et al., 2013).

The Fast Cloud Droplet Probe (FCDP, SPEC inc.) (Lance et al., 2010) was used to measure cloud droplets with a diameter and resolution of 2-50 μm and about 3 μm, respectively. It resolves the particles into 20 size bins, and the optical sizing was calibrated with known-sized standard glass beads. The liquid water content (LWC) at diameter of 2-50μm is calculated by integrating the volume at all size bins by the FCDP (Lu et al., 2012). Two-dimensional stereoscopic optical array imaging
90   probe (2D-S, SPEC Inc.) was used to record the images of cloud particles and provide the size, shape and concentration of particles. 2D-S has two orthogonal laser beams cross in the middle of the sample volume and casts the shadowgraph of particles on two linear 128-photodiode arrays when the particles transit through the laser (Lawson et al., 2006). It can measure particles of 10-1280 μm in diameter with a resolution of 10 μm, and provide detailed information of different phase particles in cloud. The precipitation particle was measured by High Volume Precipitation Spectrometer (HVPS, SPEC Inc.) (Lawson et al., 1998),
95   which is also an imaging array probe with a measure range and resolution of 150-19200 μm and 150 μm respectively. The laser beam of HVPS illuminates the imaging system, and records shadow images on the 128 elements linear photodiode array when particles pass through the sample volume. The S-band weather radar locates in Beijing (Jiang and Liu, 2014) was used

to help analyze the macro characteristics of cloud, which can detect targets within a radius of 230 km with a time and spatial resolution of 6 minutes and 1 km, respectively.

100   The Optical Array Shadow Imaging Software was used to process the raw data of 2D-S and HVPS, which can distinguish liquid drop and ice particle according to the circularity of particles (C) (Crosier et al., 2011). The C is calculated from Eq. (1):

$$C = \frac{P^2}{4\pi A},\tag{1}$$

where P and A is the perimeter around the edge of the particle and total area of the particle respectively. The perfect sphere has circularity of 1, and the other shapes have larger circularity. Irregular particles with larger circularity are counted as ice

105   particles due to the shape of ice is unlikely to be round. Considering the poorly imaged or distorted large drops/drizzles may be counted as ice particles, the circularity threshold for ice particles (irregular class) is raised to 1.2. Calculated circularity values may also be less than 1 due to the presence of images composed of only a small number of pixels, the low threshold for water drops (round class) is reduced to 0.9. In practical terms, particles with an area less than 20 pixels are classified as the small class because it is difficult to determine the shape with few pixels, and particles with an area more than 20 pixels are

110   classified as round class ($0.9 \leq C < 1.2$) or irregular class ($C \geq 1.2$). The round and irregular class are regarded as liquid drop and ice particle respectively. The round class is large droplets with diameter larger than 50 μm, and it was represented by large droplet in this study to distinguish from the cloud droplets (2-50 μm) measured by the FCDP.

    The shapes of irregular ices are further clarified as five habit classes including linear, plate, irregular, aggregate and dendrite, according to the maximum dimension, width, linearity, circularity and density of particles (Zhang et al., 2021). The mass of

115   ice is determined by particle shapes according to the approximate mass formulas for ice particles (Holroyd, 1987), and hereby the ice water content (IWC) is calculated.

    The concentration of ice nucleating particles (INP) in study was calculated by the parameterization relationship (Demott et al., 2010), which is expressed as:

$$n_{IN,T_k} = a(273.16 - T_k)^b (n_{aer,0.5})^{(c(273.16-T_k)+e)},\tag{2}$$

120   Where $a = 0.0000594$, $b = 3.33$, $c = 0.0264$, $e = 0.0033$. n_{IN,T_k} is the number concentration of INP (L^{-1}), and T_k is the temperature of cloud in degrees Kelvin, and $n_{aer,0.5}$ is the number concentration of aerosol particles with diameter larger than 0.5 μm in cloud base.

2.2 Overview of experiment

On 26th September 2017, light precipitation occurred in North China under the influence of eastward moved upper trough.

125   ERA5 reanalysis data at 08:00 BJT (UTC+8h) with a resolution of 0.25 degrees from European Centre for Medium-Range Weather Forecasts (ECMWF) showed there was a deep cold vortex system in the northwest of East Asia at 500 hPa (Fig. 1a), the bottom of which split into the shortwave trough and moved eastward, leading to a southward moved cold advection at the middle-level and conditional instability stratification (Fig. S1). Fig. 1b showed the existence of a convergence zone at 850 hPa,

where a cold front was located, and sufficient water vapor was transported through the prefrontal southerly wind. The
130 abundance of water vapor and upward motion of air led to the generation of a series of stratus clouds, and convective clouds
also appeared under the condition of instability stratification.

The study region in this research was Zhangjiakou, Hebei province (northwest of Beijing) and Beijing, and aircraft departed
from the airport in the north of Beijing in 09:54 BJT and flew to Zhangjiakou. The precipitation mainly occurred in
Zhangjiakou and became weaker after 11:00 BJT on 26th September 2017, then the precipitation band gradually moved to
135 Beijing, and weather stations observation data indicated the precipitation rate during this experiment were generally less than
1 mm/h. Fig. S2 shows the movement of the surface cold front, i.e., the convergence zone of cold and warm air masses at the
surface as determined by the temperature and wind shear measured by the ground sites. The center of the extratropical cyclone
was located in Outer Manchuria (Fig. S3), and the surface cold front extended southwestward from the position of the
extratropical cyclone to the experimental region, the experimental region was situated within the trailing end of the cold front
140 cloud system, which extended southward from the extratropical cyclone cloud system. At 09:00 to 12:00 BJT, the surface cold
front continued to move southeastward and lifted the warmer and moist air mass in front. The warm air mass ascended along
the front, forming clouds and precipitation, and the aircraft observation area was situated behind the cold front. The aircraft
sampled the clouds formed in this cyclonic system at this stage, i.e. before the surface cold front line and for the newly formed,
developing and matured clouds. This is the typical cloud system formed in this extratropical weather system over the northern
145 China.

3 Results and discussion

3.1 Identifying stages of cloud development

Four stages during the lifecycle of clouds were identified during experiment, which corresponded to the developing (S1),
mature (S2), dissipating (S3) and young cells (S4) in stratocumulus, according to their physical characteristics and radar echo.
150 Aircraft performed flight altitudes of 3.2-5.7 km at S1, 5.2-5.8 km at S2, 4.9-5.2 km at S3 and 2.1-4.9 km at S4, and AIMMS
data indicated that the 0 °C layer was at about 3.4 km. The flight tracks mapping on the composite reflectivity of precipitation
radar are shown in Fig. 2, colored by the liquid water content (LWC) from the FCDP and ice water content (IWC) from the
2D-S respectively. In developing cells, substantial LWC was detected up to 0.3 g/m^3, and the LWC and IWC at this stage
evolved with almost opposite trend (Fig. 2a1, b1). In mature cells, IWC increased up to > 0.3 g/m^3 and LWC was consumed
155 by the growth of ice particles, during when the radar reflectivity was enhanced (Fig. 2a2, b2) due to the formation of
precipitation particles in cloud. At the dissipating stage, the ice phase precipitation process occurred and the radar reflectivity
became weaker with narrowed cloud band (Fig. 2a3, b3). The last stage was young cells with rich liquid water produced from
the newly developed thermals after the front cloud bands dissipated (Fig. 2a4, b4).

Fig. 3 shows the microphysical properties of clouds and meteorological parameters along the flight track. The cross section
160 of radar reflectivity in Fig. 3a can tell the location of aircraft in cloud. The cross section of radar reflectivity along the flight

track was calculated based on the aircraft position, a vertical line was firstly determined according to the latitude and longitude of the aircraft, then obtained the azimuth angles, elevation angles, and range bins of equidistant points with a resolution of 30 meters in the vertical line, and the radar reflectivity of each equidistant points was calculated by linear interpolation in nearest neighbor combined with a vertical direction (NVI) method. The cloud-top height is indicated by red line on radar profile,

165 where the areas with radar reflectivity factor more than or equal to 5 dBZ were considered as cloud, and other areas were considered as clutter. This might give the lower estimation for the height of cloud-top because the rain radar was only sensitive to clouds with precipitations, but might not efficiently detect clouds dominated by liquid water. The size spectrum of ice showed bimodal mode with a minima diameter (d) at 180 μm (Fig. S4). The fraction of smaller ice with $d < 180$ μm ($F_{smaller\ ice}$) was defined to imply the freshly formed smaller ice which had not experienced sufficient growth (Fig. 3b).

170 The cloud-top gradually developed from S1 to S2, and the cloud-top height at S2 reached 10 km, which was the most vigorously developed clouds during the experiment. The cloud-top height at dissipating stage decreased with radar reflectivity significantly weakened. S1 was strongly turbulent with vertical wind speed varying up to ±10 m/s (Fig. 3c), which provided sufficient supersaturation of water vapor thus abundant LWC up to 0.3 g m^{-3} (Fig. 3e), it was consistent with the characteristics of developing stage. The rich LWC region occurred at the updraft region, while the ice number peaked at a valley between

175 two peaks of liquid water at the downdraft region, this implied the consumption of liquid water in producing ice.

The liquid water considerably dropped at S2, with more dominant ice than S1 (Fig. 3d, e). The distribution of large droplets and ice particles at S2 showed a bimodal distribution. The droplets at S1 grew to large droplets and were consumed by ice at S2 during the development of cloud. The strength of turbulence at S2 considerably reduced compared to S1. S3 and S4 were relatively quiescent than other stages. Similar to S2, the dissipating stage was dominated by ice but only intermittent

180 unglaciated LWC-rich clouds were present, however, the height of cloud-top at S3 was lower than S2. All above confirmed the dissipating stage of S3. S4 was likely a newly developed cell with weak radar reflectivity and the cloud-top had not reached as high as other stages. This stage was rich of liquid water with LWC up to 0.27 g/m^3 and the droplet number concentration (N_{FCDP}) reached over 1000 cm^{-3}, while there was no appreciable IWC measured at this stage. The weaker vertical wind at S4 indicated the cloud was developed slowly with sufficient LWC accumulated in cloud.

185 Fig. 4 summarizes the relation between LWC and IWC at different stages of cloud development. The general anti-correlation implied the ice to water conversion. For the newly developed cell (S4), the high LWC with less IWC (< 0.2 g m^{-3}) was predominant, and this feature was also present at developing stage. The other stages with appreciable IWC corresponded with LWC less than 0.2 g m^{-3}, indicating the cloud with different extent of glaciation. The ice-water conversion was more apparent at S2, when liquid water from the previous stage was almost consumed, with considerable cloud droplets growing into larger

190 droplets. S4 was identified as young cells, when the cloud was dominated by liquid water, and only a small amount of ice was present.

The MODIS level 2 standard product (MYD06) at 10:30 BJT (Fig. S5) showed the distribution of cloud optical depth in the study region was almost opposite to the cloud effective radius, and the area with high value of cloud optical depth corresponded to a lower cloud-top temperature. It was consistent with the distribution of precipitation, the value of cloud optical depth was

195   low in Zhangjiakou area because the liquid water was consumed during the precipitation process, and the lower cloud-top
temperature implied the vigorous development of the precipitating cloud. There were still large hydrometeors in cloud that had
not formed precipitation, thus the cloud effective radius in Zhangjiakou area was larger. The satellite results were also
consistent with the different stages of the clouds identified based on in-situ data. According to the flight track of aircraft at
different stages of clouds (Fig. 2), it was observed that during the developing stage, the cloud exhibited high optical depth and

200   small effective radius, and a warmer cloud top temperature (Fig. S5). In mature cells, there was a noticeable decrease in cloud
top temperature, and due to precipitation occurrence, the optical depth decreased while the effective radius increased. In
dissipation cells, as the cloud top height decreased and the cloud top temperature became warmer, both the optical depth and
effective radius in this region decreased, indicating the dissipation of cloud.

3.2 Ice production at different stages of cloud development

205   Fig. 5 shows the vertical profiles of microphysical properties at different stages. Fig. 5a1-a4 and Fig. 5c1-c4 are colored by
the effective diameter of droplet and $F_{smaller\ ice}$ respectively. Several target periods of S1, S2, and S4 were selected for detailed
analysis, including stages of 1.1, 1.2, 2.1, 2.2, 2.3, 4.1, 4.2, 4.3, and the corresponding periods are marked in the time series of
Fig. 3. In developing cells, the N_{FCDP} tended to decrease with the increase of height, the diameter of droplets tended to increase
(Fig. 5a1), and the concentration of large droplets (N_{Round}) increased, indicating the collision and coalescence process of

210   droplets (Fig. 5b1). The broadened droplet spectrum and increased N_{Round} in developing cells were also observed (Fig. S4).
S1.1 corresponded to high concentrations of ice (N_{Ice}) with less LWC, and S1.2 corresponded to the region with less ice and
some LWC (Fig. 5c1). The size spectrum in Fig. 6a showed the N_{FCDP} and $F_{smaller\ ice}$ at S1.2 were both higher than S1.1, and
the precipitation particles had formed at S1.1, whereas S1.2 was still dominated by smaller droplets with few precipitation
particles (Fig. 5d1). Clear similarities were observed between the two periods, the N_{round} in both periods were higher than other

215   unmarked periods at S1, and the average N_{Round} both exceeded 30 L^{-1} (Fig. 6a) and the maximum N_{Round} was over 50 L^{-1} (Fig.
5b1).

    S1.1 and S1.2 showed N_{Ice} up to 256 L^{-1} and 71 L^{-1} respectively, by considering the factor of 10, which is the uncertainty
point out by Demott et al. (2010), the observed ice concentration was still about 2 orders of magnitude higher than the
calculated INP in the corresponded temperature regime (Fig. S6). The ice shapes showed to be dominated with plate, irregular

220   and linear ice (Fig. 6a), and the 2D-S images showed the presence of H-shaped ice crystals, and the ice particles exhibited
obvious riming characteristic. The ice production of S1.1 and S1.2 appeared to be tiggered by the riming process of the large
ice, and the temperature of two periods also indicated the likely H-M process for SIP during this stage (Fig. 6a).The difference
between the two periods was that S1.1 seemed to have completed the SIP process and formed precipitation particles, the great
number of large ice at S1.1 improved the riming efficiency and increased the riming surface area, leading to more small ice

225   through H-M process and resulting in the consumption of the droplets, while there was still a large number of cloud droplets
at S1.2 with smaller number of large ice.

Cloud-top height developed to 10.1 km in mature cells, and the temperature at this stage was lower than the H-M temperature regime. The stages of 2.1, 2.2, 2.3 corresponded to areas with high, modest, low concentration of ice at S2, respectively, the N_{Round} decreased gradually from S2.1 to S2.3, and S2.2 had more cloud droplets (Fig. 5a2-d2). The size spectrum in Fig. 6b

230 showed that the N_{Ice}, N_{Round} and $F_{\text{smaller ice}}$ at S2.1 were all higher than that at S1.1. The plate, irregular and linear ice also accounted for the majority of ice at S2.1, and the riming characteristic of large ice at S2.1 was clearly shown in the images (Fig. 6b). Although the average temperature of S2.1 was as low as −11.7 ℃, the abundant large ice particles triggered the active SIP process at S2.1 with high N_{Ice} about 300 L^{-1}, indicating that the SIP process was not restricted by temperature. The period S2.2 that lacked enough large ice was still in the glaciation process, and S2.3 was difficult to trigger a more active SIP

235 process with smaller number of large ice and liquid water.

In dissipating cells, the cloud was dominated by ice and the $F_{\text{smaller ice}}$ decreased, indicating the ice production process had completed (Fig. 5a3-d3). The cloud at S4 was dominated by liquid water and classified as young cells, the cloud-top of S4 was only 5.5 km (Fig. 5a4-d4). The vertical profiles showed that periods S4.1 and S4.3 were dominated by droplets with few ice and large droplet, while the period S4.2 was composed of large droplets with few droplets. The ice particles observed at this

240 stage most likely originated from the ice nucleating process and the ice falling from the upper layer. Aircraft penetrated the cloud-top at S4.3, where several primary ice particles could be observed (Fig. 6c). The size spectrum and 2D-S images in Fig. 6c showed that large ice presented at S4.1, and ice grew through riming and Bergeron processes, while the ice at S4.2 was mainly smaller ice, which was still in the process of growth.

The large ice falling from the upper layer played a very important role in ice production process, the primary ice crystals

245 formed through the nucleation process and grew up in the upper layer or during the fall, then fell to the lower layer to trigger the ice production process. However, the number of large ice particles was not the only factor that determined the ice production process, the large droplet also played a significant role in promoting the SIP process. Fig. 7 shows the scatter plots of the corresponding distribution of N_{Ice} and N_{Round} at different stages, colored by the diameter of large droplet. There was a positive correlation between N_{Ice} and N_{Round}, where more large droplets generally corresponded to a higher N_{Ice}. Comparing

250 periods S1.1 and S1.2, it could be found that the larger large droplet tended to produce a higher N_{Ice} at the same N_{Round}, the large droplet with a diameter of 160 μm corresponded to almost 5-folds ice numbers of that of 80 μm, and Fig. 7 also clearly showed the importance of the larger large droplet to produce more ice particles at S2. Based on the above analysis, it could be inferred that when a high number of large ice particles fell from the upper layer to the lower layer, if there were abundant larger large droplets in the lower layer, the riming efficiency could be improved, and then the SIP process could be enhanced.

255 **3.3 Ice production determined by the distance to cloud-top**

Fig. 3 showed even at the same level, N_{Ice} had two orders of magnitude difference from less than unit to a few hundred per litre. This means during the aircraft penetration, the different intensity of SIP events had been experienced. The main reason causing this variability was attributed to the position of aircraft relative to the cloud-top, i.e. the distance to cloud-top (DCT) for the measurement.

260   Fig. 3b shows the time series of DCT during experiment. When penetrating a cloud turret, aircraft entered the cloud with a low DCT, reaching a higher DCT when close to convective core, leaving the cloud with a low DCT again. It therefore showed a few humps of DCT during a few penetrations of convective cells or more spread part of stratocumulus. The DCT ranged from 0.01 to 4.6 km during the experiment. Fig3b and d showed the higher DCT (2.8 and 4 km) corresponded to the peak values of N_{Ice} (256 and 300 L^{-1}) at S1 and S2. For each penetration, N_{Ice} increased dramatically when aircraft was closer to the

265   cloud core with higher DCT, but reduced when leaving. This clearly indicated the positive correlation between DCT and N_{Ice}.

Fig. 8 shows the N_{Ice} and N_{FCDP} as a function of DCT for different stages of cloud. At the developing stage, N_{Ice} significantly enhanced when DCT was above 2km, and was positively correlated with N_{Ice} up to DCT of 3km. For the mature and dissipating stage, N_{Ice} was enhanced from the cloud-top (DCT = 0.2 km) to a certain DCT but decreased when larger DCT. This implied the development of cloud-top increased N_{Ice}, but the reduced N_{Ice} close to cloud base may be due to the coalesce of ice which

270   reduced the number but enlarged the size of ice.

N_{Ice} could increase from a few dozens to a few hundreds of numbers per litre, which are all well above the estimation from INP, indicating the strong SIP. For the SIP mechanism, the temperature of S1 (−5 to −8 ℃) was in the typical H-M temperature region, while the temperature of S2 (−12 ℃) was lower than H-M temperature. Even at the same ambient temperature of measurements (because the aircraft penetration was at the same altitude), the N_{Ice} showed remarkable difference. This

275   suggested the DCT tended to be a more important factor than temperature in determining the intensity of SIP. This could be explained by the seeder-feeder mechanism occurring in the stratiform cloud precipitation (Hobbs and Locatelli, 1978; Hobbs et al., 1980; Matejka et al., 1980): when the cloud-top is higher, more primary ice form at colder temperatures and fall. The ice particles can capture smaller liquid water droplets when falling, during which they can grow and the fall speed can be accelerated. This process can considerably enhance the interaction between ice and water droplets, or among ice particles,

280   which are necessary for the occurrence of ice fracture hereby leads to the avalanche secondary ice production. The age of ice was examined as the fraction of smaller ice ($F_{smaller\ ice}$) here, with the assumption that a youngly formed ice would have smaller size. This implied the pronounced production of smaller ice by SIP processes with $F_{smaller\ ice}$ up to 70% during the developing period, while a lower $F_{smaller,ice}$ (0.2-0.6) indicated the growth of ice and smaller ice was consumed during the dissipating stage. Then the schematic plot of ice production at different stages of clouds was given (Fig. 9). The higher cloud-top leads to the

285   formation of more primary ice through the nucleation process, and the ice can grow in the upper layer and during the falling. The SIP process is triggered when the ice particles in the upper layer fall to the lower layer with supercooled water, initiating the interactions between ice and droplets. In regions with larger DCT, ice particles in the upper layer have sufficient time and distance to grow larger during falling, and the fall speed also can be accelerated, resulting in more and larger ice particles fall to the lower layer. Consequently, the intensity of SIP process becomes stronger in this region because the falling large ice

290   particles enhance the interactions between ice and droplets, as well as among ice particles.

3.4 The production rate of secondary ice

The secondary ice production rate could be estimated through the measured number size distribution of ice (Harris-Hobbs and Cooper, 1987; Crosier et al., 2011). The concentration between the length of 90-140 μm ($N_{90\text{-}140\mu m}$) was divided by the time required for ice to grow under this size. The ice grew linearly under water supersaturation at this size range and was about 1.4

295 μm/s under T = −6 ℃ (Ryan et al., 1976), resulting in around 35.7 s to grow for 50 μm (τ). Here assumed the ice numbers were in a steady state that the smaller ice at size (L) = 90 μm grew to L = 140 μm was replenished by smaller ice newly produced purely by splinters. The production rate of the smaller secondary ice could then be estimated by the ice number between this growth size limits ($N_{90\text{-}140nm}$) divided by the time required for the growth (τ). Fig. S7a showed the measured SIP rate ranged at 0.005-1.8 L^{-1} s^{-1}, generally consisted with previous observations at 0.001-1 L^{-1} s^{-1} for cumulus clouds (Harris-Hobbs and

300 Cooper, 1987), 0.043 L^{-1} s^{-1} for stratus cloud embedded with cumulus (Crosier et al., 2011), 0.14 L^{-1} s^{-1} in the mature region of cumulus (Taylor et al., 2016). Based the observation data of mixed-phase stratiform cloud system over Northern China, (Hou et al., 2021) estimated the SIP rate and found the highest concentration of ice splinter could reach 1000 L^{-1} in five minutes, which implied that the average SIP rate could up to 3.3 L^{-1} s^{-1}. Fig. S7c and Fig. S8 showed the rate was positively correlated with the number concentration of large ice and large droplet at S1-S3.

305 The above analysis showed the importance of collision-coalescence process in producing the enhancement of ice number concentration. The collision-coalescence model had been previously used to calculate the production rate of secondary ice. It was essentially determined by the collision-coalescence between graupel and droplet above certain size. It was long established in the laboratory that only droplet > 25 μm in diameter could produce secondary ice when rimmed on the graupel. The SIP rate could therefore be calculated from the collision-coalescence process among graupel and droplet (Reisner et al., 1998), and

310 the model calculated equation is described as:

$$P = \pi/4 \cdot (D_{\text{graupel}} + D_{\text{droplet}})^2 N(D_{\text{graupel}}) N(D_{\text{droplet}}) E |U_{\text{graupel}} - U_{\text{droplet}}| , \qquad (3)$$

where D_{graupel} and D_{droplet} are the effective diameter (which is the third divided by the second moment of size distribution) of graupel and droplet respectively, and $N(D_{\text{graupel}})$ and $N(D_{\text{droplet}})$ are the number concentration of graupel and droplet respectively; U_{graupel} and U_{droplet} represent the terminal velocities, which are calculated as the absolute difference between graupel and droplet,

315 as $U_{\text{graupel}} = 7 \times 10^2 D_{\text{graupel}}$, $U_{\text{droplet}} = 3 \times 10^7 D_{\text{droplet}}$. E is the collection efficiency among the size bins of graupel and droplet, which was assumed to be 1 for the first instance but would be discussed as following. The ice particle with $d > 250$ μm was considered as graupel which was able to efficiently capture droplet (Harris-Hobbs and Cooper, 1987). Here the effective radius (Re) was used to represent the size distribution of graupel/droplet within a time window to simplify the calculation of collision among size bins. The Re was used rather than median mass value from the size distribution was because the former was determined

320 by the cross section of particles (and the collection by collision-coalescence process was also determined by area), and weighted towards larger particles. Ice particles were observed to be mostly rimed in images, hereby all ices were considered to be graupels that already accreted by small droplets (i.e. $d < 13$ μm), but not calculated the fraction of rimmed surface (Harris-Hobbs and Cooper, 1987). Considering that the observation here was actually after the SIP process was initialized, when the

smaller cloud droplets had been considerably consumed and most graupels were rimed, the number of large droplets was the
325 limited factor for SIP, and therefore used to calculate the modelled SIP rate.

Fig. S7a shows the time series of modelled SIP rate, which was well correlated with measured SIP (correlation coefficient
was 0.86), the ratio between Re of graupels and large droplets (Re_{Round} / $Re_{Graupel}$) ranged from 0.1-0.8 (Fig. S7b). Fig. 10
investigated the correlation between measured and modelled SIP rate, colored by Re_{Round} / $Re_{Graupel}$. According to Eq. (3), the
collection efficiency $E = 1$ was firstly considered which gave the upper limit for the calculation, but any other circumstances
330 would cause $E < 1$ and reduced the model results. The model was closed to the observation when Re_{Round} / $Re_{Graupel}$ ranged at
0.4-1 (slope=0.94), but model started to overestimate compared to observation when Re_{Round} / $Re_{Graupel}$ decreased (shown by
the datapoints grouped as different levels of Re_{Round} / $Re_{Graupel}$). This clearly indicated reduced E when reduced Re_{Round} / $Re_{Graupel}$.
E was then further adjusted to give the modelled SIP rate matched with observation at different levels of Re_{Round} / $Re_{Graupel}$,
shown in the sub-plot of Fig. 10. A linearly increased collection efficiency was found, when E increased from 0.2 to 1 with
335 Re_{Round} / $Re_{Graupel}$ increased from 0.1 to 0.7. This was consisted with the theory of droplet collision, when the collector particle
approaches the droplet, the droplet tends to follow the streamline around the collector particle and may avoid collision (Wallace
and Hobbs, 2006; Pruppacher and Klett, 2010). The collision efficiency was small when the collector particle was much larger
than the droplet, because too small particles would follow the streamline around collector particle due to small inertia, and the
collision efficiency increased with increased droplet size because droplets with greater inertia tended to follow a straight line.
340 The results here implied that the SIP rate could be well explained by the collision theory between rimed graupel and large
droplet, and the availability of both numbers and the chance for their collision were the factors in determining the SIP rate.

4 Conclusion

In this study, we investigated the ice production and phase transformation of stratocumulus during an extratropical cyclone
over the North China Plain, through the in-situ measurements of the microphysical properties. The aircraft penetrated four
345 stages during the lifecycle of the clouds including the developing, mature, dissipating and young cells. In the developing cells,
high N_{Ice} and strong turbulence were observed, and the LWC-rich region was presented in the updraft region. The cloud-top
further developed in mature cells with reduced turbulence, the higher glaciation extent was observed at this stage with N_{Ice}
reaching up to 300 L^{-1}. The dissipating cells were dominated by ice but only intermittent unglaciated LWC-rich clouds, with
a lower cloud-top compared to previous stages. The young stage was rich of LWC with the lowest cloud-top. The number
350 concentration of ice was found to frequently well exceeds that from ice nucleation, reaching up to a few hundred per litre,
indicating the strong secondary ice production (SIP).

The seeder-feeder process was found to extend the SIP process beyond the slightly supercooled temperature region for the
typically considered H-M process. The intensity of SIP was to the first order determined by the numbers of graupel and droplets,
because the collision and coalescence among these hydrometers necessitate the fracture of ice. The modelled and measurement-
355 based calculation showed appropriate treating the size distribution hereby the determination of collection efficiency will

improve the modelling of the SIP rate. Importantly, the results showed the generally enhanced SIP when larger distance to cloud-top, which means once the cloud-top reached sufficient height, the initialized ice from nucleation may boost the avalanche glaciation process when falling ice reached lower levels in cloud. It should be noted that whether the falling hydrometeors were the ones generated by the ice production process or were about to participate in the ice production process

360   at the same level, may never be separated due to the short time-scale of the collision process. However, this is a continuous process which may involve both the already-formed and ongoing-happening particles, and we have observed or modelled is an overall net production of ice. The ice particles falling from aloft increase the numbers of graupels and collision chance between graupel and droplets, and then trigger the SIP process, therefore the seeder-feeder and SIP process may occur simultaneously after SIP process has initialized. The results about the microphysical properties of clouds with convective cells

365   under different stages may improve the understanding of the key processes in controlling the cloud glaciation and precipitation process, and also help find the region of supercooled water of clouds for the weather modification work.

370

Data availability

The data in this study are available from the authors upon request.

Author contribution

375   YD and DL analyzed the data and wrote the manuscript, and this work was completed under the guidance of DL, MH and DD. DeZ, PT, WX, WZ, JS and FW contributed to the aircraft data processing and analysis. DW, XL and YC performed the synoptic analysis. BP, YJ contributed to the satellite data analysis. DoZ and YH contributed to the radar data processing and analysis. RZ conducted the shape classification of 2D-S images.

Competing interests

At least one of the (co-)authors is a member of the editorial board of *Atmospheric Chemistry* and *Physics*. The authors also have no other competing interests to declare.

Acknowledgements

385   This research was supported by the National Natural Science Foundation of China (Grant Nos. 42205093, 42075084, 42005078).

References

Bacer, S., Sullivan, S. C., Sourdeval, O., Tost, H., Lelieveld, J., and Pozzer, A.: Cold cloud microphysical process rates in a global chemistry–climate model, Atmospheric Chemistry and Physics, 21, 1485-1505, 10.5194/acp-21-1485-2021, 2021.

Beswick, K. M., Gallagher, M. W., Webb, A. R., Norton, E. G., and Perry, F.: Application of the Aventech AIMMS20AQ airborne probe for turbulence measurements during the Convective Storm Initiation Project, Atmospheric Chemistry and Physics, 8, 5449-5463, 2008.

Cai, Y., Snider, J. R., and Wechsler, P.: Calibration of the passive cavity aerosol spectrometer probe for airborne determination of the size distribution, Atmospheric Measurement Techniques, 6, 2349-2358, 10.5194/amt-6-2349-2013, 2013.

Cantrell, W. and Heymsfield, A.: Production of Ice in Tropospheric Clouds: A Review, Bulletin of the American Meteorological Society, 86, 795-808, 10.1175/bams-86-6-795, 2005.

Crosier, J., Choularton, T. W., Westbrook, C. D., Blyth, A. M., Bower, K. N., Connolly, P. J., Dearden, C., Gallagher, M. W., Cui, Z., and Nicol, J. C.: Microphysical properties of cold frontal rainbands†, Quarterly Journal of the Royal Meteorological Society, 140, 1257-1268, 10.1002/qj.2206, 2013.

Crosier, J., Bower, K. N., Choularton, T. W., Westbrook, C. D., Connolly, P. J., Cui, Z. Q., Crawford, I. P., Capes, G. L., Coe, H., Dorsey, J. R., Williams, P. I., Illingworth, A. J., Gallagher, M. W., and Blyth, A. M.: Observations of ice multiplication in a weakly convective cell embedded in supercooled mid-level stratus, Atmospheric Chemistry and Physics, 11, 257-273, 10.5194/acp-11-257-2011, 2011.

DeMott, P. J., Prenni, A. J., Liu, X., Kreidenweis, S. M., Petters, M. D., Twohy, C. H., Richardson, M. S., Eidhammer, T., and Rogers, D. C.: Predicting global atmospheric ice nuclei distributions and their impacts on climate, Proc Natl Acad Sci U S A, 107, 11217-11222, 10.1073/pnas.0910818107, 2010.

Field, P. R., Lawson, R. P., Brown, P. R. A., Lloyd, G., Westbrook, C., Moisseev, D., Miltenberger, A., Nenes, A., Blyth, A., Choularton, T., Connolly, P., Buehl, J., Crosier, J., Cui, Z., Dearden, C., DeMott, P., Flossmann, A., Heymsfield, A., Huang, Y., Kalesse, H., Kanji, Z. A., Korolev, A., Kirchgaessner, A., Lasher-Trapp, S., Leisner, T., McFarquhar, G., Phillips, V., Stith, J., and Sullivan, S.: Secondary Ice Production - current state of the science and recommendations for the future, Meteorological Monographs, 10.1175/amsmonographs-d-16-0014.1, 2016.

Hallett, J. and Mossop, S. C.: Production of Secondary ice particles during the riming process, Nature, 249, 26–28, doi:10.1038/249026a0., 1974.

Harris-Hobbs, R. L. and Cooper, W. A.: Field evidence supporting quantitative predictions of secondary ice production rates, journal of the atmospheric sciences, 44, 1071-1082, 1987.

Hobbs, P. V. and Locatelli, J. D.: Rainbands, Precipitation Cores and Generating Cells in a Cyclonic Storm, Journal of Atmospheric Sciences, 35, 230-241, 1978.

Hobbs, P. V., Matejka, T. J., Herzegh, P. H., Locatelli, J. D., and Houze , R. A.: The Mesoscale and Microscale Structure and Organization of Clouds and Precipitation in Midlatitude Cyclones. I: A Case Study of a Cold Front, Journal of Atmospheric Sciences, 37, 568-596, 1980.

Hogan, R. J., Field, P. R., Illingworth, A. J., Cotton, R. J., and Choularton, T. W.: Properties of embedded convection in warm-frontal mixed-phase cloud from aircraft and polarimetric radar, Quarterly Journal of the Royal Meteorological Society: A journal of the atmospheric sciences, applied meteorology and physical oceanography, 128, 451-476, 2002.

Holroyd, E. W.: Some Techniques and Uses of 2D-C Habit Classification Software for Snow Particles, Journal of Atmospheric and Oceanic Technology, 4, 498–511, 1987.

Hou, T., Lei, H., He, Y., Yang, J., Zhao, Z., and Hu, Z.: Aircraft Measurements of the Microphysical Properties of Stratiform Clouds with Embedded Convection, Advances in Atmospheric Sciences, 38, 966-982, 10.1007/s00376-021-0287-8, 2021.

Hou, T., Chen, B., Zhou, X., Zhao, C., Feng, Q., Yan, F., Zhou, W., Cui, Y., Du, Y., Li, Z., Zhao, D., and Ma, X.: Aircraft-based observations of ice concentrations in a midlatitude mixed-phase stratiform cloud system with embedded convection, Atmospheric Research, 281, 10.1016/j.atmosres.2022.106471, 2023.

Huang, Y., Blyth, A. M., Brown, P. R. A., Choularton, T. W., Connolly, P., Gadian, A. M., Jones, H., Latham, J., Cui, Z., and Carslaw, K.: The development of ice in a cumulus cloud over southwest England, New Journal of Physics, 10, 10.1088/1367-2630/10/10/105021, 2008.

Jiang, Y. and Liu, L.: A test pattern identification algorithm and its application to CINRAD/SA(B) data, Advances in Atmospheric Sciences, 31, 331-343, 10.1007/s00376-013-2315-9, 2014.

Kanji, Z. A., Ladino, L. A., Wex, H., Boose, Y., Burkert-Kohn, M., Cziczo, D. J., and Krämer, M.: Overview of Ice Nucleating Particles, Meteorological Monographs, 58, 1.1-1.33, 10.1175/amsmonographs-d-16-0006.1, 2017.

Korolev, A., DeMott, P. J., Heckman, I., Wolde, M., Williams, E., Smalley, D. J., and Donovan, M. F.: Observation of secondary ice production in clouds at low temperatures, Atmospheric Chemistry and Physics, 22, 13103-13113, 10.5194/acp-22-13103-2022, 2022.

Korolev, A., Heckman, I., Wolde, M., Ackerman, A. S., Fridlind, A. M., Ladino, L. A., Lawson, R. P., Milbrandt, J., and Williams, E.: A new look at the environmental conditions favorable to secondary ice production, Atmospheric Chemistry and Physics, 20, 1391-1429, 10.5194/acp-20-1391-2020, 2020.

Korolev, A., McFarquhar, G., Field, P. R., Franklin, C., Lawson, P., Wang, Z., Williams, E., Abel, S. J., Axisa, D., Borrmann, S., Crosier, J., Fugal, J., Krämer, M., Lohmann, U., Schlenczek, O., Schnaiter, M., and Wendisch, M.: Mixed-Phase Clouds: Progress and Challenges, Meteorological Monographs, 58, 5.1-5.50, 10.1175/amsmonographs-d-17-0001.1, 2017.

Lance, S., Brock, C. A., Rogers, D., and Gordon, J. A.: Water droplet calibration of the Cloud Droplet Probe (CDP) and in-flight performance in liquid, ice and mixed-phase clouds during ARCPAC, Atmospheric Measurement Techniques, 3, 1683-1706, 10.5194/amt-3-1683-2010, 2010.

Lau, K. M. and Wu, H. T.: Warm rain processes over tropical oceans and climate implications, Geophysical Research Letters, 30, 10.1029/2003gl018567, 2003.

Lawson, R. P., Stewart, R. E., and Angus, L. J.: Observations and Numerical Simulations of the Origin and Development of Very Large Snowflakes, Journal of the Atmospheric Sciences, 55, 1998.

Lawson, R. P., Woods, S., and Morrison, H.: The Microphysics of Ice and Precipitation Development in Tropical Cumulus Clouds, Journal of the Atmospheric Sciences, 72, 2429-2445, 10.1175/jas-d-14-0274.1, 2015.

Lawson, R. P., O'Connor, D., Zmarzly, P., Weaver, K., Baker, B., Mo, Q., and Jonsson, H.: The 2D-S (Stereo) Probe: Design and Preliminary Tests of a New Airborne, High-Speed, High-Resolution Particle Imaging Probe, Atmospheric and Oceanic Technology, 23, 1462–1477, 2006.

Li, Z., Lau, W. K. M., Ramanathan, V., Wu, G., Ding, Y., Manoj, M. G., Liu, J., Qian, Y., Li, J., Zhou, T., Fan, J., Rosenfeld, D., Ming, Y., Wang, Y., Huang, J., Wang, B., Xu, X., Lee, S. S., Cribb, M., Zhang, F., Yang, X., Zhao, C., Takemura, T., Wang, K., Xia, X., Yin, Y., Zhang, H., Guo, J., Zhai, P. M., Sugimoto, N., Babu, S. S., and Brasseur, G. P.: Aerosol and monsoon climate interactions over Asia, Reviews of Geophysics, 54, 866-929, 10.1002/2015rg000500, 2016.

Liu, Q., Liu, D., Gao, Q., Tian, P., Wang, F., Zhao, D., Bi, K., Wu, Y., Ding, S., Hu, K., Zhang, J., Ding, D., and Zhao, C.: Vertical characteristics of aerosol hygroscopicity and impacts on optical properties over the North China Plain during winter, Atmospheric Chemistry and Physics, 20, 3931-3944, 10.5194/acp-20-3931-2020, 2020.

Lloyd, G., Dearden, C., Choularton, T. W., Crosier, J., and Bower, K. N.: Observations of the Origin and Distribution of Ice in Cold, Warm, and Occluded Frontal Systems during the DIAMET Campaign, Monthly Weather Review, 142, 4230-4255, 10.1175/mwr-d-13-00396.1, 2014.

Locatelli, J. D., Stoelinga, M. T., and Woods, C. P.: Size Spectra of Snow Particles Measured in Wintertime Precipitation in the Pacific Northwest, Journal of the Atmospheric Sciences, 65, 189-205, 10.1175/2007jas2243.1, 2008.

Lohmann, U. and Feichter, J.: Global indirect aerosol effects: a review, Atmos. Chem. Phys., 5, 715–737, https://doi.org/10.5194/acp-5-715-2005, 2005.

Lu, C., Liu, Y., Niu, S., and Vogelmann, A. M.: Observed impacts of vertical velocity on cloud microphysics and implications for aerosol indirect effects, Geophysical Research Letters, 39, 10.1029/2012gl053599, 2012.

Matejka, T. J., Houze, R. A., and Hobbs, P. V.: Microphysics and dynamics of clouds associated with mesoscale rainbands in extratropical cyclones, Quarterly Journal of the Royal Meteorological Society, 106, 29–56, 10.1002/qj.49710644704 1980.

McFarquhar, G. M., Baumgardner, D., and Heymsfield, A. J.: Background and Overview, Meteorological Monographs, 58, v-ix, 10.1175/amsmonographs-d-16-0018.1, 2017.

Mossop, S. C.: Secondary ice particle production during rime growth: The effect of drop size distribution and rimer velocity, Quarterly Journal of the Royal Meteorological Society, 111, 1113-1124, 1985.

Mülmenstädt, J., Sourdeval, O., Delanoë, J., and Quaas, J.: Frequency of occurrence of rain from liquid-, mixed-, and ice-phase clouds derived from A-Train satellite retrievals, Geophysical Research Letters, 42, 6502-6509, 10.1002/2015gl064604, 2015.

Pruppacher, H. R. and Klett, J. D.: Microphysics of Clouds and Precipitation, Springer2010.

Rangno, A. L. and Hobbs, P. V.: Ice particles in stratiform clouds in the Arctic and possible mechanisms for the production of high ice concentrations, Journal of Geophysical Research: Atmospheres, 106, 15065-15075, 10.1029/2000jd900286, 2001.

Reisner, J., Rasmussen, R. M., and Bruintjes, R. T.: Explicit forecasting of supercooled liquid water in winter storms using the MM5 mesoscale model, Quarterly Journal of the Royal Meteorological Society, 124, 1071–1107, https://doi.org/10.1002/qj.49712454804, 1998.

Ryan, B. F., Wishart, E. R., and Shaw, D. E.: Growth Rates and Densities of Ice Crystals between −3°C and −21°C, Journal of Atmospheric Sciences, 33, 842-850, 1976.

Taylor, J. W., Choularton, T. W., Blyth, A. M., Liu, Z., Bower, K. N., Crosier, J., Gallagher, M. W., Williams, P. I., Dorsey, J. R., Flynn, M. J., Bennett, L. J., Huang, Y., French, J., Korolev, A., and Brown, P. R. A.: Observations of cloud microphysics and ice formation during COPE, Atmospheric Chemistry and Physics, 16, 799-826, 10.5194/acp-16-799-2016, 2016.

Tian, P., Liu, D., Zhao, D., Yu, C., Liu, Q., Huang, M., Deng, Z., Ran, L., Wu, Y., Ding, S., Hu, K., Zhao, G., Zhao, C., and Ding, D.: In situ vertical characteristics of optical properties and heating rates of aerosol over Beijing, Atmospheric Chemistry and Physics, 20, 2603-2622, 10.5194/acp-20-2603-2020, 2020.

Wallace, J. M. and Hobbs, P. V.: Atmospheric Science: An Introductory Survey, Elsevier2006.

Wang, D., Duan, Y., Liu, Y., Liang, Z., Liu, C., Zhao, Y., Zhang, Y., Yin, J., and Wang, H.: A case study of the November 2012 mixed rain-snow storm over North China, Acta Meteorologica Sinica, 27, 601-625, 10.1007/s13351-013-0512-1, 2014.

Yang, J., Lei, H., and Hou, T.: Observational evidence of high ice concentration in a shallow convective cloud embedded in stratiform cloud over North China, Advances in Atmospheric Sciences, 34, 509-520, 10.1007/s00376-016-6079-x, 2017.

Zhang, R., Li, H., Zhou, X., Li, H., Hu, X., and Xia, Q.: Shape Recognition of DMT Airborne Cloud Particle Images and Its Application, JOURNAL OF APPLIED METEOROLOGICAL SCIENCE 32, 735-747, 2021.

500   Zhao, C., Chen, Y., Li, J., Letu, H., Su, Y., Chen, T., and Wu, X.: Fifteen-year statistical analysis of cloud characteristics over China using Terra and Aqua Moderate Resolution Imaging Spectroradiometer observations, International Journal of Climatology, 39, 2612-2629, 10.1002/joc.5975, 2019.

Zuo, D., Liu, D., Zhao, D., Yang, L., Chen, Y., Zhou, W., Huang, M., He, H., Tian, P., Du, Y., Xiao, W., Li, R., Li, J., Gao, Y., Lu, J., Tang, Q., Wang, W., and Ding, D.: Liquid water determination by airborne millimeter cloud radar and in-situ size distribution measurements, Atmospheric Research, 284, 10.1016/j.atmosres.2023.106607, 2023.

505

510

515

520

525

530
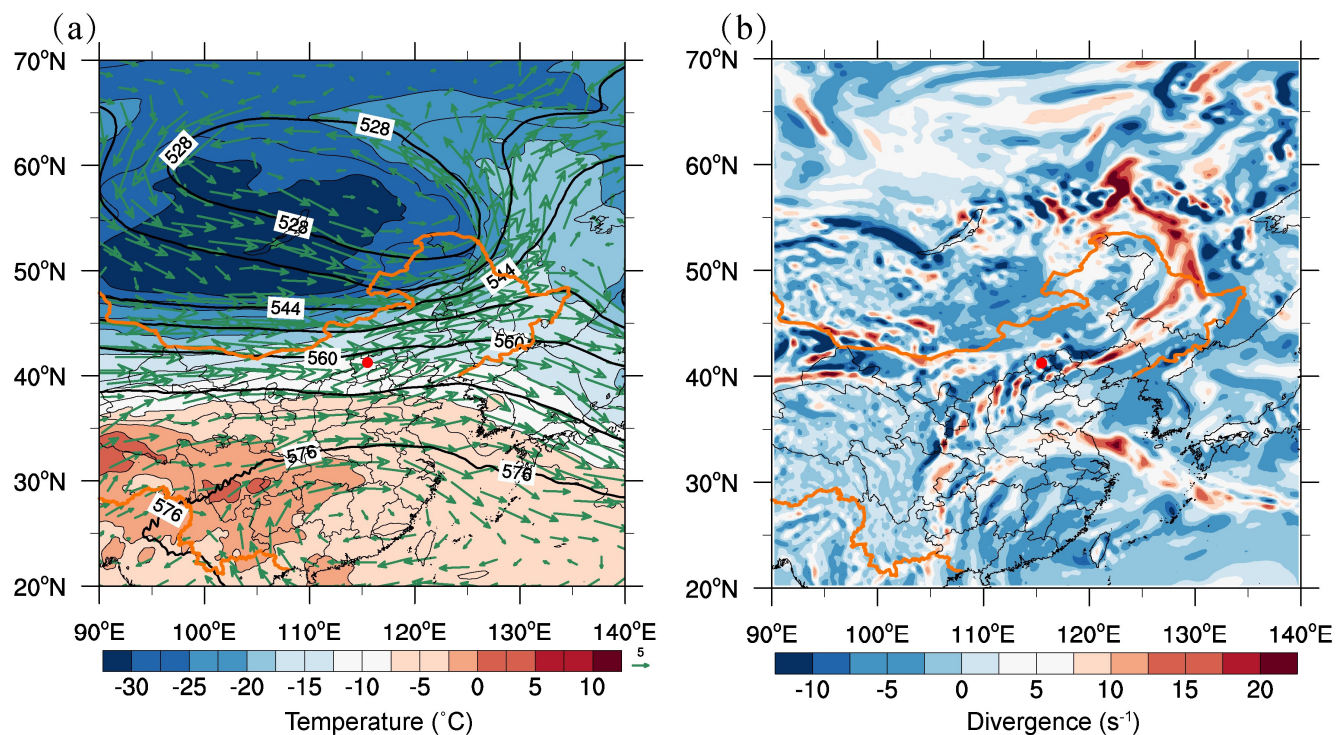
Figure 1: Synoptic overview during experiment. (a) The 500hPa temperature (color), height field (contour), wind field (arrow) at 08:00 (UTC+8h) on September 26th, 2017; (b) 850hPa divergence field (color), relative humidity (blue line, only >80% is shown). The experimental region is indicated by the red dot on each plot.
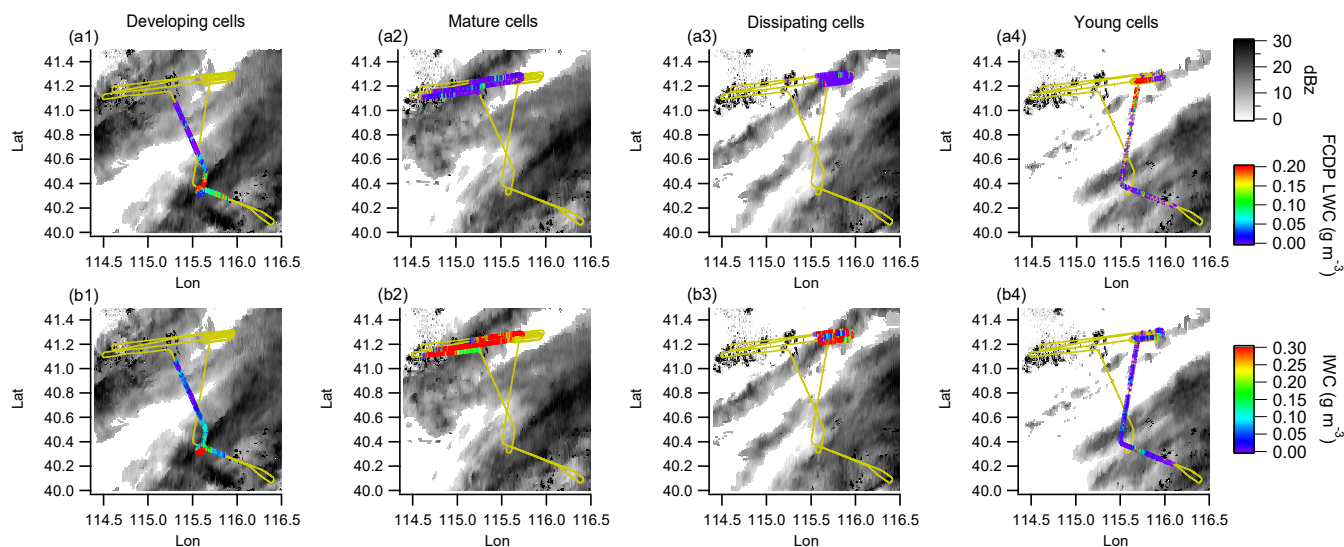
Figure 2: Flight tracks mapping on the composite reflectivity of S-band precipitation radar at different stages of clouds (from left to right). (a) colored by liquid water content (LWC) from the FCDP, (b) colored by ice water content (IWC) from the 2D-S.

555

560

565

570
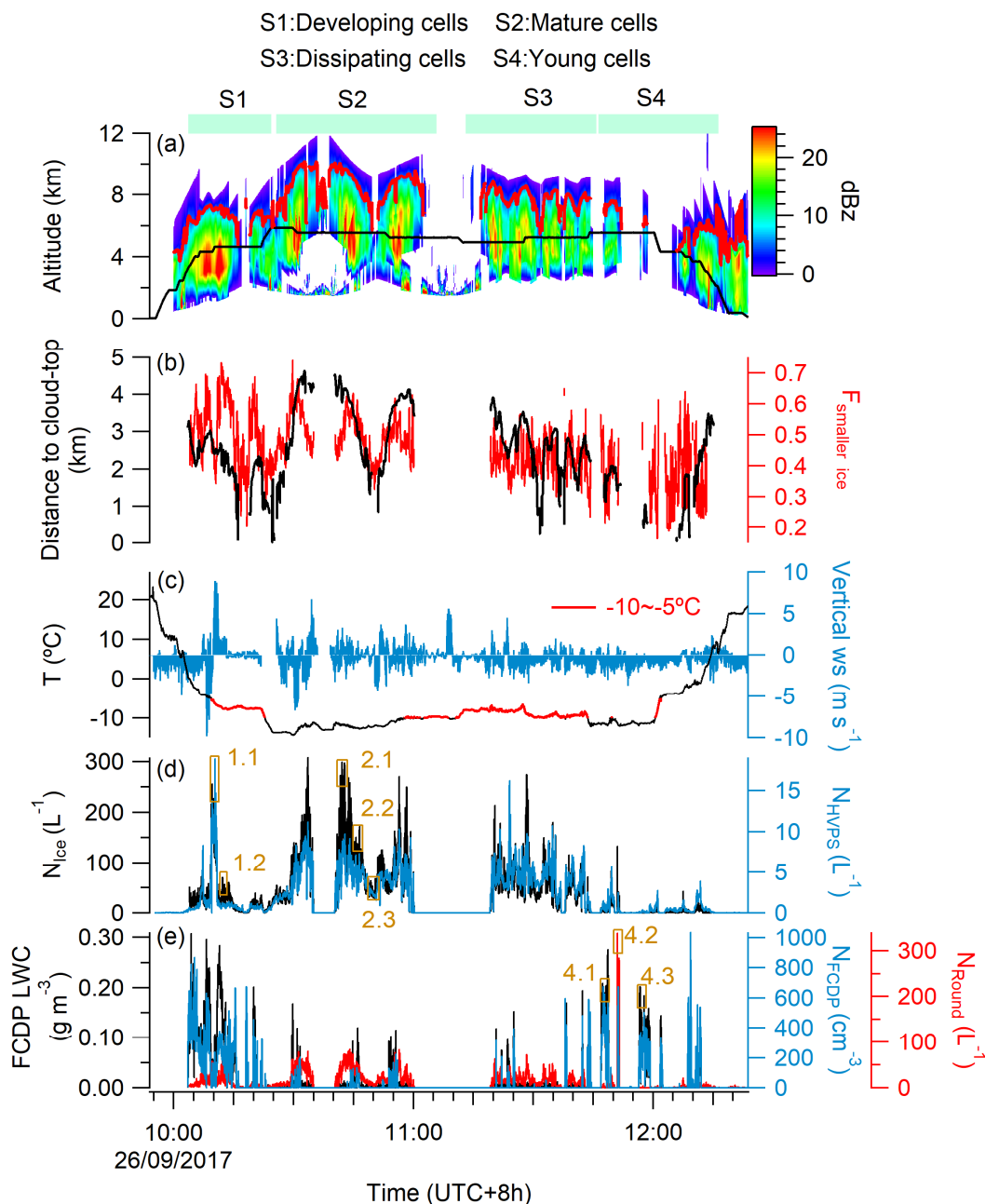
Figure 3: Time series of key cloud properties along the flight track. (a) Vertical profile of radar reflectivity from the ground S-band precipitation radar collocating with the flight path. (b)The distance to cloud-top of aircraft and smaller ice (d < 180 μm) number fraction ($F_{smaller\ ice}$). (c) Ambient temperature and vertical wind speed. (d) Ice number concentration (N_{Ice}) from the 2D-S and precipitation particle number concentration (N_{HVPS}) from the HVPS. (e) LWC and cloud droplet number concentration (N_{FCDP}) from the FCDP, and the large droplet number concentration (N_{Round}) from the 2D-S. The targeting periods are indexed for further analysis.
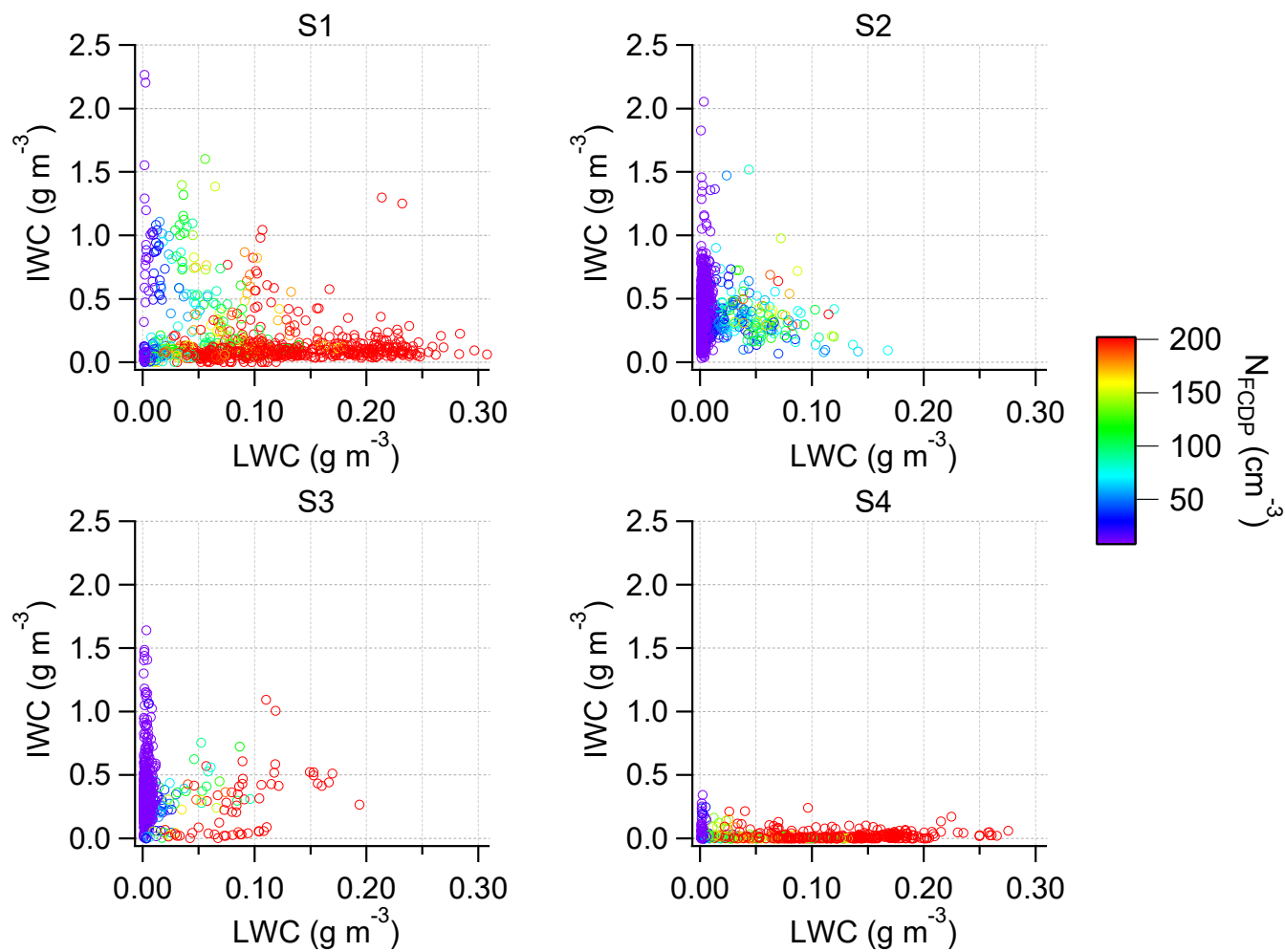
Figure 4: LWC as a function of IWC at different stages of clouds, colored by N_{FCDP}.
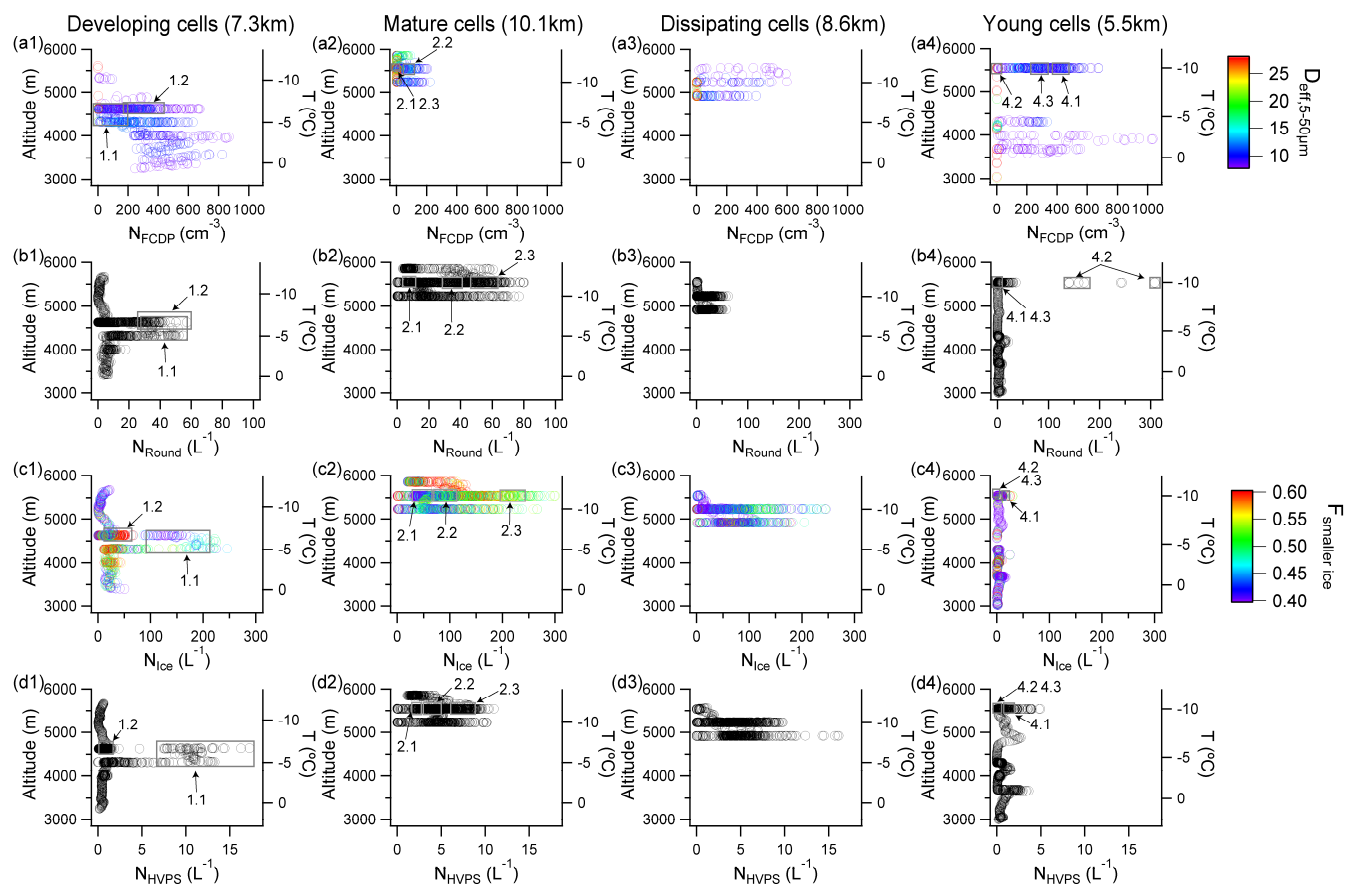
590

Figure 5: Vertical distributions of hydrometeors at different stages of clouds. (a) N_{FCDP} colored by the effective diameter of droplet (5-50 μm), (b) N_{Round}, (c) N_{Ice} colored by $F_{smaller\ ice}$, (d) N_{HVPS}. The corresponding indexed events in timeseries are marked in this figure, and the cloud-top height was indicated in title brackets.

595

600
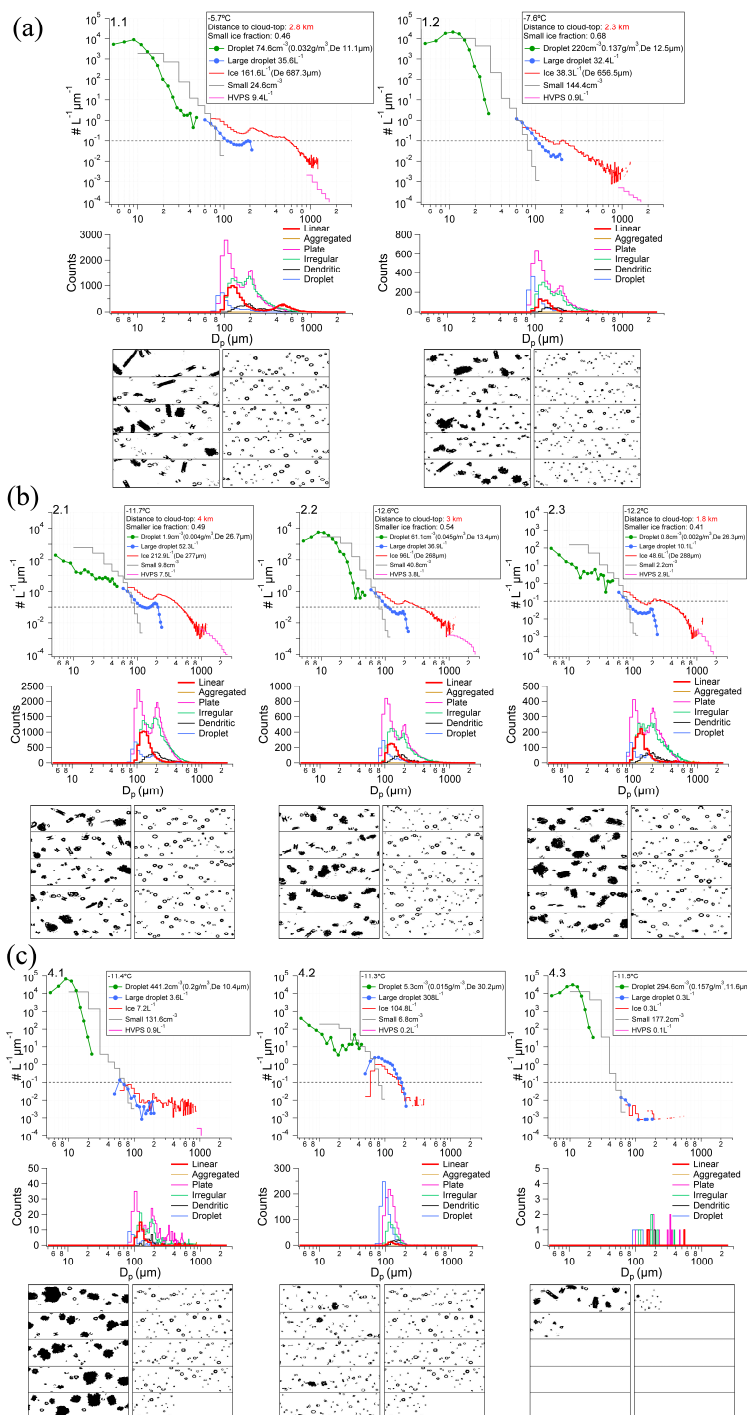
Figure 6: Particle size spectrum from airborne particle spectrum probes, the 2D-S images and the shape classification results of 2D-S images (a) periods S1.1 and S1.2, (b) periods S2.1, S2.2 and S2.3, (c) periods S4.1, S4.2 and S4.3.
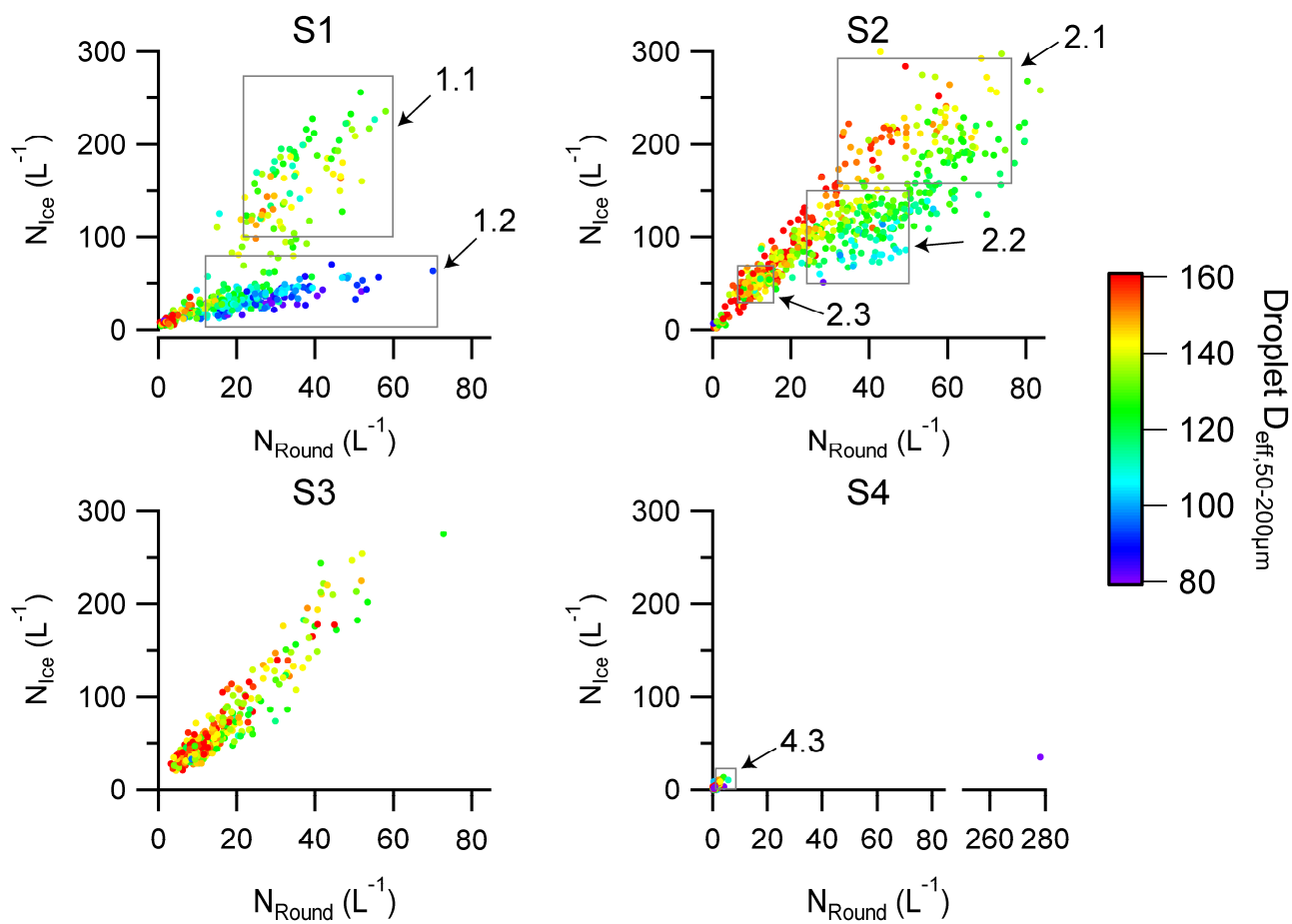
Figure 7: N_{Round} **as a function of** N_{Ice} **at different stages, colored by the diameter of large droplet (50-200 μm).**

610

615
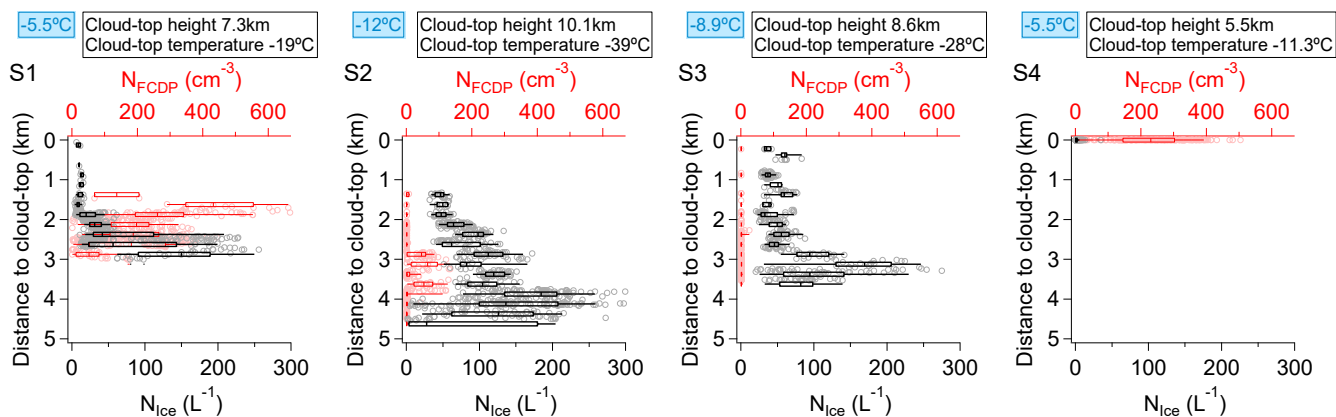
Figure 8: N_{FCDP} **and** N_{Ice} **as a function of distance to cloud-top. Gray circled markers and black boxes represent** N_{Ice}**, light red circled markers and red boxes represent** N_{FCDP}**. Whiskers extend to 5th and 95th percentiles, boxes encompass 25th to 75th percentiles and 50th percentiles are vertical lines. The blue box in each figure indicates the temperature of aircraft measurements.**
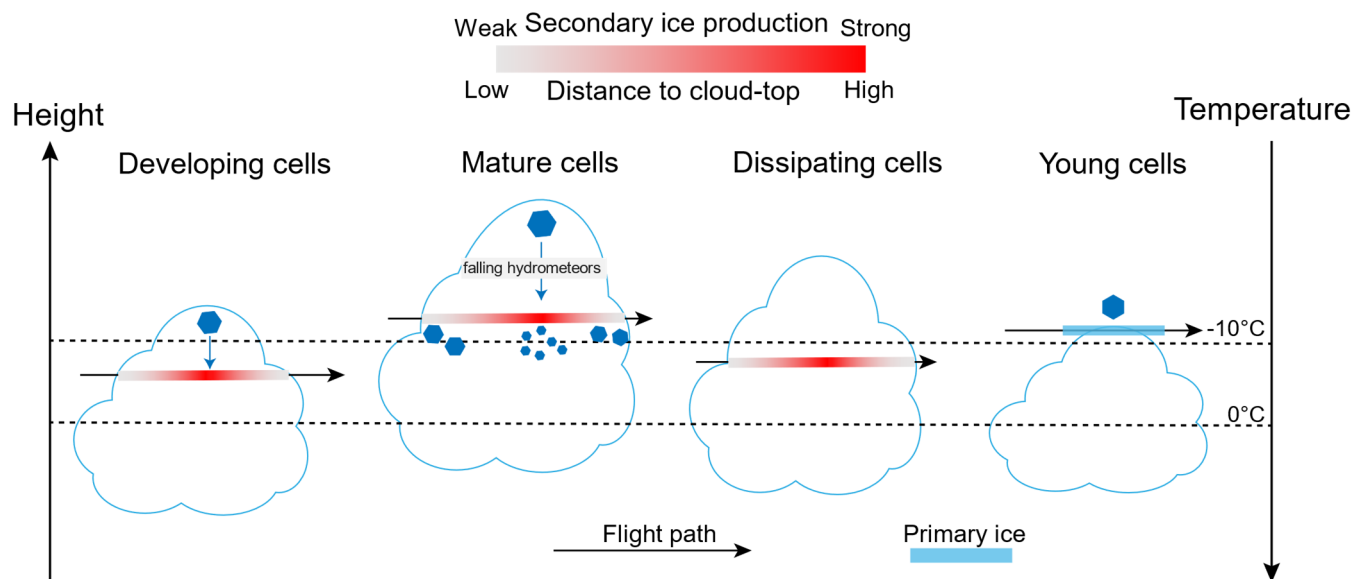
Figure 9: Schematic show of ice production at different stages of clouds.

645

650

655

660
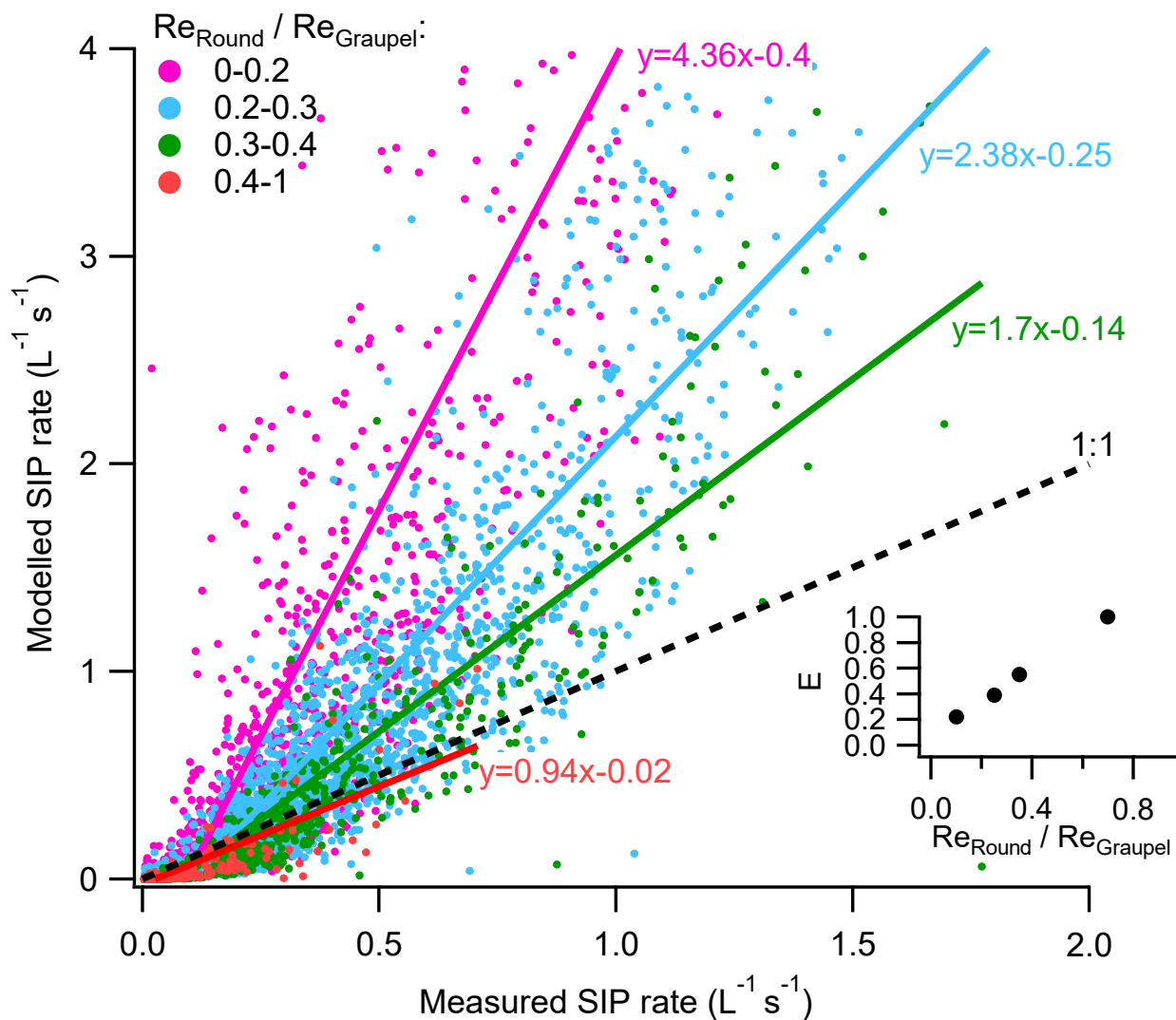
Figure 10: Measured against modelled secondary ice production (SIP) rate. The scatter plot is classified and colored by the ratio of
665 **effective radius between large droplet and graupel (Re_Round / Re_graupel), and each group of data points is performed least-square linear**
fitting. The sub-plot shows the derived collection efficiency between graupel and large droplet at different Re_Round / Re_graupel.